Stacking-Dependent Electronic States in the Natural van der Waals Heterostructure 4Hb-$TaS_{2-x}Se_x$

Min Shan (单敏)[1], Zhen Wang (王臻)[2], Linpeng Nie (聂林鹏)[1], Dan Zhao (赵丹)[1], Ziji Xiang (项子雾)[1,5], Jinglei Zhang (张警蕾)[3], Jing Tao (陶靖)[2**], Tao Wu (吴涛)[1,2,4,5**] and Xianhui Chen (陈仙辉)[1,2,4,5**]

[1]Hefei National Research Center for Physical Sciences at the Microscale, University of Science and Technology of China, Hefei, Anhui 230026, China.
[2]Department of Physics, University of Science and Technology of China, Hefei, Anhui 230026, China.
[3]Anhui Province Key Laboratory of Condensed Matter Physics at Extreme Conditions, High Magnetic Field Laboratory, Chinese Academy of Sciences, Hefei 230031, China
[4]Collaborative Innovation Center of Advanced Microstructures, Nanjing University, Nanjing 210093, China.
[5]Hefei National Laboratory, University of Science and Technology of China, Hefei, Anhui 230088, China.

**Corresponding authors. Email:

jingtao1975@ustc.edu.cn; wutao@ustc.edu.cn; chenxh@ustc.edu.cn

Abstract

Natural van der Waals (vdW) materials offer a fertile ground for exploring stacking-dependent physics analogous to moiré superlattices. In this study, we investigate lightly Se-doped 4Hb-TaS_2 single crystals, which consist of alternating 1T and 1H layers. Two types of crystals, S1 and S2, synthesized under identical growth conditions, exhibit distinct crystalline structures and electronic states. While both retain the 4Hb framework, S2 possesses a relative in-plane stacking shift between adjacent layers compared to S1. This structural modification enhances the star-of-David charge-density-wave (CDW) transition temperature from 315 K in S1 to 327 K in S2 and alters the interlayer CDW registry. Crucially, S2 displays a rare nonlinear Hall response featuring two plateau-like characteristics, starkly contrasting with the behavior observed in S1. A phenomenological multiband analysis suggests that these plateau-like characteristics may be qualitatively associated with electron–hole compensation in the transport response. Our findings establish interlayer stacking as a potent tuning parameter for manipulating emergent electronic states in natural vdW systems.

Keywords: van der Waals heterostructures, stacking modulation, electron microscopy, electron transport

PACS: 74.62.Bf, 75.47.-m, 71.45.Lr

1. Introduction

Layered van der Waals (vdW) materials provide an ideal platform for probing the interplay between lattice and electronic degrees of freedom, giving rise to various collective quantum states such as charge density waves (CDWs) and superconductivity.[1,2] In these structurally sensitive systems, stacking serves as a pivotal parameter that governs interlayer coupling and the low-energy electronic states, thereby modulating physical properties.[3–7] Such effects are prominently demonstrated in twisted moiré two-dimensional systems, where minute variations in the relative alignment between adjacent layers can induce strongly correlated electronic states and unconventional superconductivity.[8–10]

Beyond artificially assembled structures, natural van der Waals heterostructures (vdWHs) offer an intrinsic setting for exploring stacking-dependent phenomena.[11–15] Since adjacent layers in these systems are primarily bound by weak vdW interactions, variations in their stacking arrangements can directly tune their physical properties. 4Hb-TaS_2 is a representative natural vdWH composed of alternating octahedral 1T-TaS_2 and trigonal 1H-TaS_2 layers along the *c*-axis.[16] The 1T layers undergo a star-of-David CDW transition near 315 K, associated with correlated electronic states. Conversely, the 1H layers are metallic, exhibiting a low-temperature CDW order around 22 K and becoming superconducting near 3 K. The coexistence of structurally and electronically distinct layers in 4Hb-TaS_2 has led to exotic physical phenomena, including unconventional superconductivity, enigmatic magnetic memory, and topological edge states.[17–28]

Given that these emergent properties are intimately tied to interlayer coupling, they are expected to be highly sensitive to the stacking arrangement. This raises a compelling question: can a relative 1T/1H stacking shift modulate the low-energy electronic states while preserving the fundamental 4Hb framework? To address this, we systematically investigated the physical properties of lightly Se-doped 4Hb-TaS_2 single crystals using structural characterization and transport measurements.

2. Methods

X-ray diffraction (XRD) measurements were performed using a SmartLab diffractometer with Cu Kα radiation. Atomic-resolution high-angle annular dark-field (HAADF) and annular bright-field scanning transmission electron microscopy (ABF-STEM) images were acquired using a JEOL Grand ARM300 microscope operated at 300 kV at room temperature (~300 K). Selected-area electron diffraction (SAED) patterns were acquired at room temperature (~300 K). The chemical compositions were examined by energy-dispersive X-ray spectroscopy (EDS) using a GeminiSEM 500 system. Electrical transport measurements were performed in the Physical Property Measurement System (PPMS). Resistivity and magnetoresistance (MR) were measured using a standard four-probe method with the current applied in the *ab* plane. Hall measurements were carried out in a Hall bar geometry with the magnetic field swept from −14 T to +14 T along the *c* axis. The Hall resistivity (ρ_{xy}) was obtained by antisymmetrizing the field-dependent data.

3. Results and Discussion

a) Crystal Growth and Structural Characterization

Two types of 4Hb-$TaS_{2-x}Se_x$ single crystals, denoted as S1 and S2, were obtained under identical nominal growth conditions via the chemical vapor transport method using I_2 as the transport agent. A polycrystalline precursor with a nominal molar ratio of Ta:S:Se = 1:1.98:0.02 was prepared by heating high-purity Ta, S, and Se powders in an evacuated quartz tube at 780 °C for 5 days. The precursor was subsequently ground, mixed with I_2, and sealed in a quartz tube. The tube was placed in a two-zone furnace with the source and growth zones maintained at 780 °C and 680 °C, respectively, for 30 days. After quenching, plate-like single crystals with typical dimensions of approximately 1 × 1.5 × 0.1 mm^3 were obtained.

XRD patterns and HAADF-STEM images confirm that both S1 and S2 retain the fundamental 4Hb framework. Temperature-dependent single-crystal XRD measurements at 350 K and 300 K reveal sharp (*00l*) reflections without discernible secondary phases, indicating high phase purity for both types [Figs. 1(b) and 1(c)]. However, the (*00l*) reflections of S2 are systematically shifted to lower 2θ angles relative to those of S1 [Figs. 1(d) and 1(e)]. The extracted c-axis lattice parameters at 300 K (350 K) are ~23.72 Å (~23.70 Å) for S1 and ~23.82 Å (~23.79 Å) for S2. This indicates that while both types exhibit a slight c-axis expansion upon cooling across the CDW transition, S2 maintains a larger c-axis parameter than S1 by approximately 0.1 Å at both temperatures.

To resolve this structural discrepancy at the atomic scale, HAADF-STEM was employed to image the projected atomic columns of S1 and S2 along the [001] zone axis. Due to the Z-contrast mechanism, the bright spots primarily correspond to the projected Ta atomic columns. As shown in Fig. 1(f), S1 displays a regular trigonal array of bright Ta columns, consistent with the conventional 4Hb stacking where Ta sites in adjacent 1T and 1H layers overlap along the c direction. In contrast, S2 [Fig. 1(g)] exhibits a denser hexagonal array of bright Ta columns throughout the entire observed area, clearly deviating from the ideal alignment in S1. As illustrated in Fig. 1(h), this feature likely arises from relative interlayer sliding between adjacent 1T and 1H layers. Consequently, the Ta sites in the two layers are no longer fully aligned along the c direction, with one set of projected Ta columns displaced toward the projected S sites of the adjacent layer. A similar trigonal-to-hexagonal array transition induced by stacking shifts has been previously reported in 1T-TaS_2.[30] Thus, our HAADF-STEM observations identify S1 as the conventional 4Hb configuration and S2 as a stacking-shifted 4Hb variant. This further suggests that relative interlayer sliding may allow multiple stacking configurations within the 4Hb framework. Notably, a recent study reported a similar enhancement of the CDW transition temperature in pristine 4Hb-TaS_2, which may be attributed to the formation of a similar stacking-shifted variant as observed in our S2 type. [29]

b) Modulation of CDW States and Transport Properties

Having identified the distinct stacking arrangements, we examined their influence on the star-of-David CDW state in the 1T layers. Figures 2(a) and 2(d) show the temperature dependence of the in-plane resistivity (ρ_{ab}) for S1 and S2. Both types exhibit metallic behavior and a pronounced resistive anomaly at high temperatures, corresponding to the formation of the star-of-David CDW. Here, the CDW transition temperature is defined by the onset of the resistive anomaly. For S1, the CDW transition occurs at approximately 315 K, consistent with pristine 4Hb-TaS_2.[16] In contrast, the CDW transition temperature in S2 is significantly enhanced to approximately 327 K.

To determine whether the stacking shift influences the relative arrangement of the star-of-David CDW superstructures between neighboring 1T layers, SAED patterns were acquired from S1 and S2 along the [001] zone axis at room temperature (~300 K). As shown in Figs. 2(b) and 2(e), both types retain the fundamental diffraction spots of the 4Hb lattice, indicating that the average 4Hb framework is preserved. In S1, CDW-related satellite reflections are consistent with those of the star-of-David CDW in the 1T layers. In S2, the fundamental reflections and CDW satellite positions remain nearly unchanged, while the relative intensities of the CDW satellite spots are redistributed, suggesting a relative phase shift in the CDW stacking between neighboring 1T layers. We compared the experimental results with representative stacking models discussed in the literature and with the corresponding simulated electron diffraction patterns shown in Fig. S5. [31,32] The comparison shows that S1 is best described by the $-\alpha-\alpha-$ stacking phase [Fig. 2(c)], whereas S2 is best described by the $-\alpha-\gamma-$ stacking phase [Fig. 2(f)]. These results demonstrate that the stacking shift in S2 modifies the relative arrangement of the CDW superstructures, which is associated with the enhanced CDW transition temperature.

c) Low-Temperature Magnetotransport

To investigate the impact of stacking on the low-energy electronic states, we compared the low-temperature magnetotransport properties of S1 and S2. Figures 3(a) and 3(e) show the MR, defined as MR = $[\rho_{xx}(B)-\rho_{xx}(0)]/\rho_{xx}(0)\times 100\%$. Both types exhibit positive MR without saturation up to 14 T. However, the low-temperature MR curves of S1 exhibit pronounced curvature, whereas S2 displays a quasi-linear field dependence. We then extracted the temperature dependence of the MR at 14 T, as shown in Figs. 3(b) and 3(f). The MR of both samples increases markedly below 100 K. Figures 3(c) and 3(g) depict the magnetic field dependence of the ρ_{xy} for S1 and S2. At high temperatures, ρ_{xy} exhibits a positive and linear response in both types, indicative of hole-dominated transport. Upon cooling, the curves gradually deviate from this linear dependence. For S1, this deviation becomes apparent around 30 K, resembling the nonlinear Hall response observed in pristine 4Hb-TaS_2.[33,34] In contrast, S2 displays a more complex nonlinear behavior, with the deviation emerging at a higher temperature of approximately 50 K. At low

temperatures, ρ_{xy} in S2 is strongly suppressed in the low-field region, developing a distinct plateau-like feature (Fig. S6). As the field increases, ρ_{xy} gradually rises but exhibits another weakly field-dependent region around 5–8 T, before recovering a pronounced positive slope at higher fields (Fig. S7). This multistage nonlinear Hall response is absent in S1, highlighting the distinct low-temperature electronic states in the two types.

To quantitatively characterize this behavior, we extracted the effective Hall coefficient ($R_{H,eff}$) from the slopes of ρ_{xy} in two field regions: the low-field coefficient ($R_{H,LF}$) from −0.5 T to 0.5 T, and the high-field coefficient ($R_{H,HF}$) from 13 T to 14 T. For S1 [Fig. 3(d)], $R_{H,LF}$ and $R_{H,HF}$ coincide at high temperatures but begin to separate around 30 K, with $R_{H,LF}$ increasing rapidly. For S2 [Fig. 3(h)], the separation occurs near 50 K. Upon further cooling, $R_{H,HF}$ remains positive and weakly temperature-dependent, whereas $R_{H,LF}$ is rapidly suppressed and approaches zero below 10 K. This contrasting evolution underscores the pronounced suppression of the low-field Hall signal in S2.

d) Multiband Analysis of the Hall Response

Motivated by the complex low-energy electronic structure of 4Hb-TaS_2, we performed a phenomenological analysis using the multiband Drude model.[34–36] The resistivity components ρ_{xx} and ρ_{xy} were converted into longitudinal conductivity σ_{xx} and Hall conductivity σ_{xy}:

$$\sigma_{xx}(B) = \frac{\rho_{xx}}{\rho_{xx}^2 + \rho_{xy}^2} = \sum_i \frac{n_i e \mu_i}{1 + (\mu_i B)^2}$$

$$\sigma_{xy}(B) = \frac{\rho_{xy}}{\rho_{xx}^2 + \rho_{xy}^2} = \sum_i s_i \frac{n_i e \mu_i^2 B}{1 + (\mu_i B)^2}$$

where n_i and μ_i are the effective carrier density and mobility of the i-th transport channel, and $s_i = \pm 1$ denotes the hole- or electron-type contribution. For the low-temperature regime (≤ 30 K), σ_{xx} and σ_{xy} were fitted simultaneously. At high temperatures (≥ 100 K), a single-band fit was applied to ρ_{xy}.

At 5 K, the data for S1 can be reasonably described by a three-channel model with one electron-type and two hole-type channels, consistent with pristine 4Hb-TaS_2 [Figs. 4(a) and 4(b)].[34] In contrast, the complex multistage nonlinear σ_{xy} of S2 cannot be captured by the three-channel model. Instead, a four-channel model was adopted to describe both the plateau-like feature in σ_{xy} and the overall field dependence of σ_{xx} [Figs. 4(e) and 4(f)], indicating more complex effective transport contributions in S2. Representative fitting parameters at 5 K are summarized in Table S3. Specifically, the nearly vanishing low-field Hall signal in S2 can be qualitatively associated with electron–hole compensation. In the low-field region, electron-type and hole-type contributions with opposite signs and comparable magnitudes may cancel out,

suppressing the net Hall signal while maintaining finite σ_{xx}. Increasing the magnetic field breaks this compensation condition gradually, leading to the observed multistage response.

It should be noted that the multiband fitting mainly captures the dominant features of the transport response, while deviations between the experimental data and the fitted curves remain in both σ_{xx} and the Hall response [Figs. 4(b), 4(f), and Fig. S6]. These deviations highlight the limitation of applying a simple multiband Drude model to such complex low-temperature transport behavior. Therefore, the present multiband analysis should be viewed as a qualitative and phenomenological description rather than a complete microscopic explanation. In this sense, the fitting suggests possible electron–hole compensation in S2, but it should not be regarded as direct evidence for a distinct microscopic band structure. Further direct probes, such as ARPES, are needed to clarify whether the distinct Hall response between S1 and S2 originates from a detectable band-structure modification or from other transport-related mechanisms.

e) Role of Stacking Modulation

Our analysis indicates that the distinct nonlinear Hall responses can be phenomenologically described in terms of multiple effective transport contributions. Combined with the enhanced low-temperature MR, this suggests a significant evolution of the magnetotransport properties. In pristine 4Hb-TaS_2, such behavior has been attributed to the low-temperature CDW transition in the 1H layers.[34] For our Se-doped samples, although the resistive anomaly of the 1H-layer CDW is suppressed, a residual CDW state likely persists, which may contribute to the nonlinear Hall response at low temperatures. [37,38]

Crucially, the markedly different behavior between S1 and S2 demonstrates that the low-energy electronic states are highly sensitive to the stacking arrangement.[13,39–42] The structural characterization confirms that S2 is a stacking-shifted 4Hb variant. This shift modifies the interlayer alignment between the 1T and 1H layers. Consequently, it alters the relative registry between the star-of-David CDW superstructure in the 1T layers and the residual CDW modulations in the adjacent 1H layers, thereby modulating the CDW-related low-energy electronic states probed by magnetotransport. In this scenario, S1 retains a multiband response similar to the pristine 4Hb-TaS_2, whereas the stacking-shifted S2 can be phenomenologically described by introducing an additional effective electron-type contribution. Nevertheless, whether this phenomenological difference reflects a detectable microscopic band-structure modification remains to be clarified by further direct probes. Beyond the transport response, the stacking modulation in S2 may provide an intriguing opportunity to explore how structural configurations influence the correlated magnetic and superconducting states reported in 4Hb-TaS_2, including Kondo-related behavior, chiral order, nematicity, and time-reversal-symmetry-breaking states.[22–26,43] Further microscopic magnetic, spectroscopic, and superconducting-state investigations will be valuable for revealing how these correlated states evolve under stacking modulation.

4. Conclusion

In summary, we demonstrate that the natural vdWH 4Hb-$TaS_{2-x}Se_x$ serves as an ideal platform for exploring how stacking modulates CDW states and low-temperature magnetotransport properties. Our results show that the stacking arrangement not only tunes the star-of-David CDW transition temperature and the interlayer CDW registry but also induces an exotic multistage nonlinear Hall response with pronounced low-field plateaus. The suppressed low-field Hall signal in S2 points to a distinct low-temperature electronic state, whose microscopic origin remains to be clarified in future studies. These findings establish interlayer stacking as a critical degree of freedom for tuning physical properties in natural vdWHs.

Acknowledgments:

We thank useful discussion with Zhenyu Wang and Junfeng He. This work is supported by the National Natural Science Foundation of China (Grant Nos. 12325403, 12034004, 12161160316, and 12488201), the National Key R&D Program of the MOST of China (Grant No. 2022YFA1602601), the Chinese Academy of Sciences under contract No. JZHKYPT-2021-08, the CAS Project for Young Scientists in Basic Research (Grant No. YBR-048), and the Innovation Program for Quantum Science and Technology (Grant No. 2021ZD0302800).

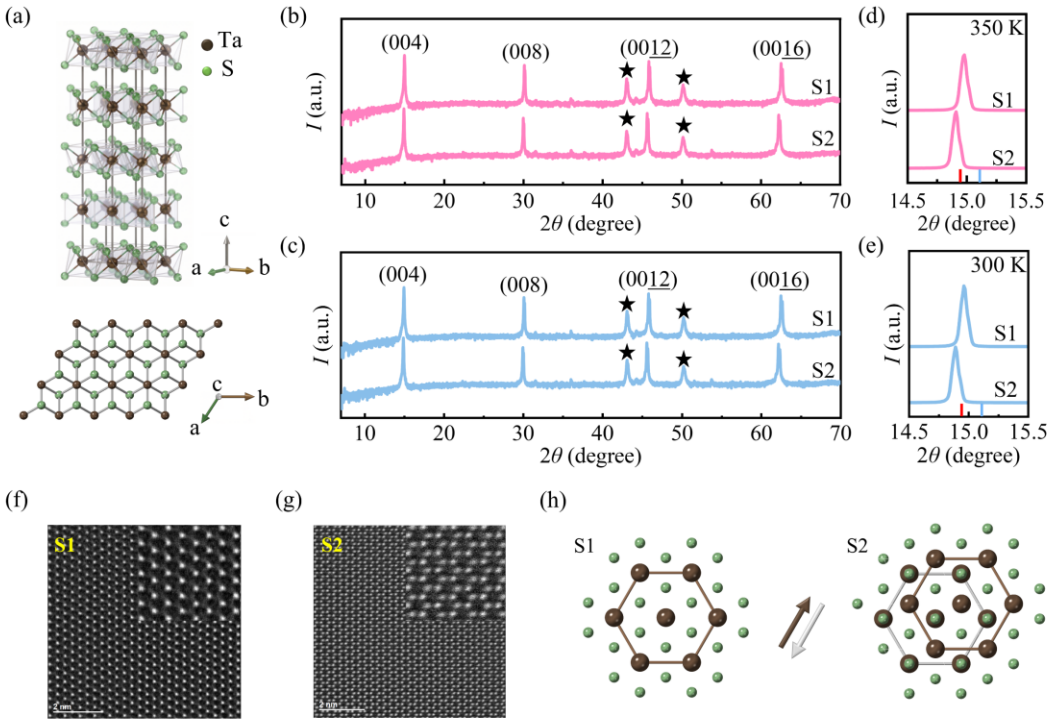


Fig. 1. Structural characterization of 4Hb-$TaS_{2-x}Se_x$ single crystals. (a) Schematic crystal structure of 4Hb-TaS_2. The upper and lower panels display the side and top views, respectively. **(b, c)** Single-crystal XRD patterns of S1 and S2 measured at **(b)** 350 K and **(c)** 300 K, respectively. Intensities are plotted on a logarithmic scale. To prevent potential sample degradation or reaction upon air exposure at elevated temperatures, the samples were mounted in an airtight holder during measurements. The weak peaks indicated by the black stars originate from the airtight sample holder. For comparison, room-temperature XRD patterns measured without the airtight holder are provided in Fig. S3. **(d, e)** Enlarged views of the (004) reflections at **(d)** 350 K and **(e)** 300 K, respectively. The red and blue bars mark the reference positions for the pristine 4Hb-TaS_2 (004) and 1T-TaS_2 (002) reflections, respectively.[29] **(f, g)** HAADF-STEM images of **(f)** S1 and **(g)** S2 acquired along the [001] zone axis at room temperature (~300 K). The upper-right insets show enlarged views of the selected regions. **(h)** Schematic illustration comparing the stacking configuration in S1 with the relative stacking shift between adjacent 1T and 1H layers in S2.

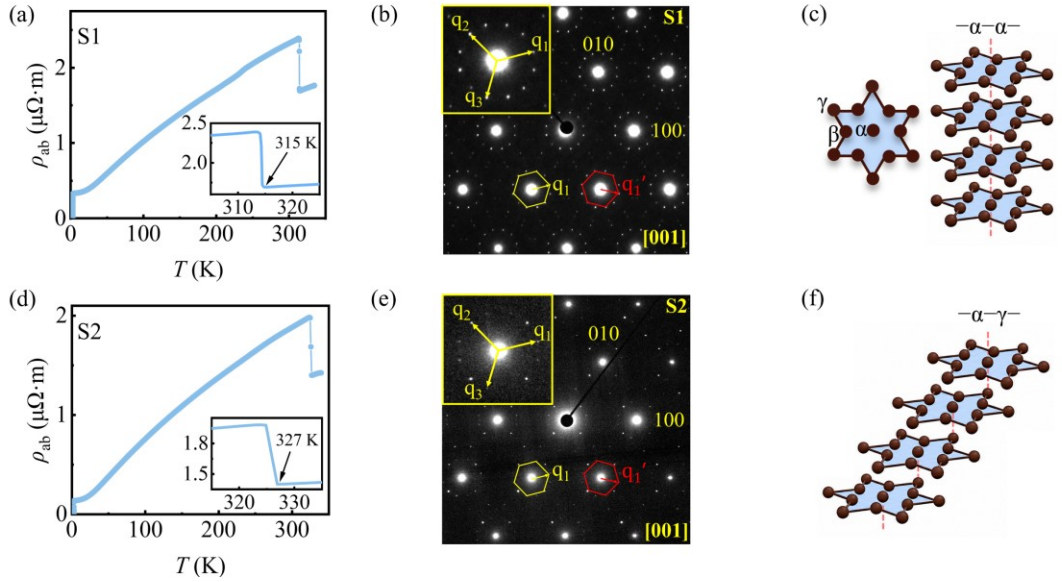


Fig. 2. Star-of-David CDW transition and superstructure arrangements in S1 and S2. (a, d) Temperature dependence of the in-plane resistivity ρ_{ab} for **(a)** S1 and **(d)** S2. The insets display the CDW transitions. The CDW transition temperature is defined by the onset of the resistivity anomaly, giving 315 K for S1 and 327 K for S2. **(b, e)** Selected-area electron diffraction (SAED) patterns of **(b)** S1 and **(e)** S2 taken along the [001] zone axis at room temperature (~300 K). The upper-left insets magnify representative CDW satellite reflections. The arrows q_1, q_2, and q_3 denote the three CDW wavevectors of one domain. The red and yellow polygons mark two mirror-related sets of CDW satellite reflections. For clarity, only the representative vectors q_1 and q_1' are indicated for the two domains. **(c, f)** Schematic illustrations of the star-of-David CDW stacking configurations corresponding to **(c)** the *–α–α–* stacking phase and **(f)** the *–α–γ–* stacking phase. The α, β, and γ labels denote distinct Ta sites within a single star-of-David cluster, as detailed in the inset of **(c)**. The red dashed lines indicate the centers of the star-of-David clusters.

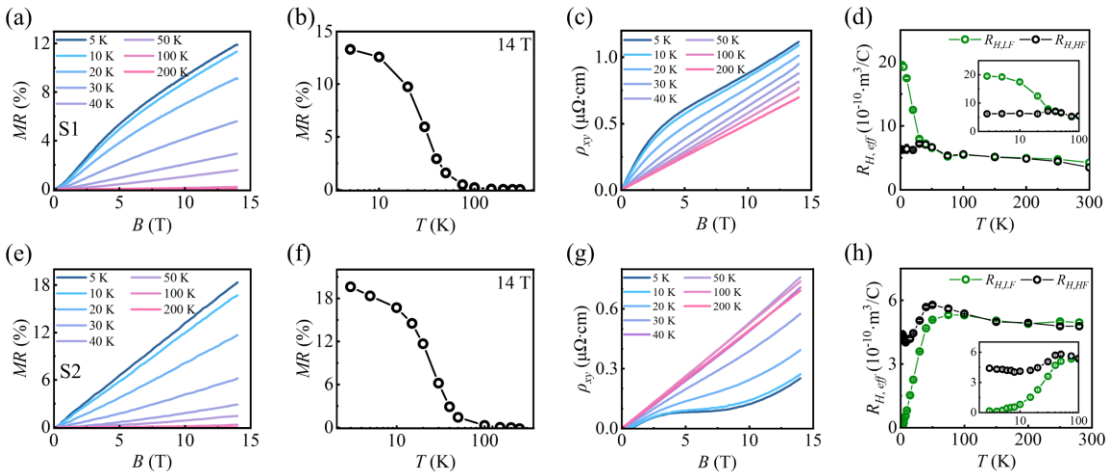


Fig. 3. Magnetotransport properties of 4Hb-$TaS_{2-x}Se_x$ single crystals. (a–d) Magnetotransport properties of S1. **(e–h)** Magnetotransport properties of S2. **(a, e)** Magnetoresistance (MR) of **(a)** S1 and **(e)** S2 at selected temperatures. **(b, f)** Temperature dependence of the MR at 14 T for **(b)** S1 and **(f)** S2. **(c, g)** Magnetic-field dependence of the Hall resistivity ρ_{xy} for **(c)** S1 and **(g)** S2 at selected temperatures. **(d, h)** Temperature dependence of the effective Hall coefficients $R_{H,eff}$ for **(d)** S1 and **(h)** S2. $R_{H,LF}$ and $R_{H,HF}$ were extracted from the slopes of ρ_{xy} in the low-field (−0.5 T to 0.5 T) and high-field (13 T to 14 T) regions, respectively. The insets in **(d)** and **(h)** display enlarged views of the low-temperature region.

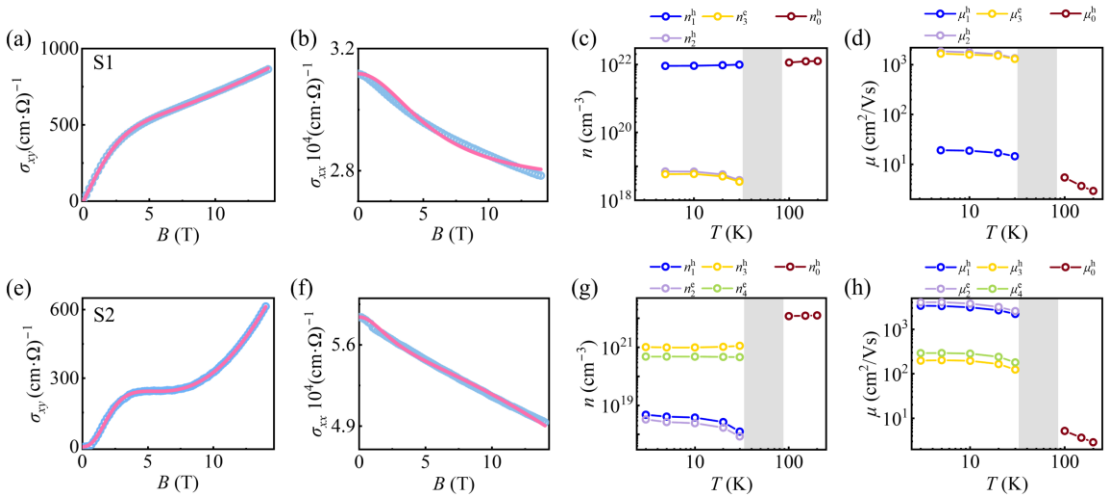


Fig. 4. Multiband analysis of magnetotransport properties in 4Hb-$TaS_{2-x}Se_x$ single crystals. **(a–d)** Fitting analysis for S1. **(e–h)** Fitting analysis for S2. **(a, e)** Representative fitting results of σ_{xy} at 5 K for **(a)** S1 and **(e)** S2. **(b, f)** Representative fitting results of σ_{xx} at 5 K for **(b)** S1 and **(f)** S2. Open blue symbols and solid red lines represent experimental data and fitting results based on the multiband Drude model, respectively. **(c, g)** Temperature dependence of the carrier density n_i extracted from the fitting analysis for **(c)** S1 and **(g)** S2. **(d, h)** Temperature dependence of the mobility μ_i extracted from the fitting analysis for **(d)** S1 and **(h)** S2. The superscripts h and e denote hole-type and electron-type transport channels, respectively. The gray shaded regions indicate intermediate-temperature regimes that were not included in the fitting analysis. At low temperatures, a three-channel model was used to describe S1, whereas a four-channel model was adopted for S2. The high-temperature transport can be approximately described by a single hole-type channel.

References

[1] Geim A K and Grigorieva I V 2013 *Nature* **499** 419.

[2] Novoselov K S, Mishchenko A, Carvalho A and Castro Neto A H 2016 *Science* **353** aac9439.

[3] He J G, Hummer K and Franchini C 2014 *Phys. Rev. B* **89** 075409.

[4] Liu K H, Zhang L M, Cao T, Jin C H, Qiu D, Zhou Q, Zettl A, Yang P D, Louie S G and Wang F 2014 *Nat. Commun.* **5** 4966.

[5] Akashi R, Ochi M, Bordács S, Suzuki R, Tokura Y, Iwasa Y and Arita R 2015 *Phys. Rev. Appl*. **4** 014002.

[6] Suzuki R, Sakano M, Zhang Y J, Akashi R, Morikawa D, Harasawa A, Yaji K, Kuroda K, Miyamoto K, Okuda T and Ishizaka K 2014 *Nat. Nanotechnol*. **9** 611.

[7] Wang Z N, Lv Y P, Chang H N and Zhang J 2025 *Chin. Phys. B* **34** 107201.

[8] Cao Y, Fatemi V, Fang S, Watanabe K, Taniguchi T, Kaxiras E and Jarillo-Herrero P 2018 *Nature* **556** 43.

[9] Cao Y, Fatemi V, Demir A, Fang S, Tomarken S L, Luo J Y, Sanchez-Yamagishi J D, Watanabe K, Taniguchi T, Kaxiras E, Ashoori R C and Jarillo-Herrero P 2018 *Nature* **556** 80.

[10] Bistritzer R and MacDonald A H 2011 *Proc. Natl. Acad. Sci. U.S.A*. **108** 12233.

[11] Manzeli S, Ovchinnikov D, Pasquier D, Yazyev O V and Kis A 2017 Nat. Rev. Mater. 2 17033.

[12] Katzke H, Tolédano P and Depmeier W 2004 *Phys. Rev. B* **69** 134111.

[13] Ding Z Y, Wang Y H, Li R, Gao J J, Jiang J L, Tang J, Han Y Y, Xu Q, Zhu J F, Tu W Q, Lu W J, Yang Y G, Li Z H, Gao X Y, Qu Z, Sun Y P, Luo X, Yang X P, Xu H, Xiong Y M and Cao L 2026 *Natl. Sci. Rev.* **13** nwag246.

[14] Ritschel T, Berger H and Geck J 2018 *Phys. Rev. B* **98** 195134.

[15] Darancet P, Millis A J and Marianetti C A 2014 *Phys. Rev. B* **90** 045134.

[16] Di Salvo F J, Bagley B G, Voorhoeve J M and Waszczak J V 1973 *J. Phys. Chem. Solids* **34** 1357.

[17] Wen C, Gao J, Xie Y, Zhang Q, Kong P, Wang J, Jiang Y, Luo X, Li J, Lu W and Sun Y P 2021 *Phys. Rev. Lett.* **126** 256402.

[18] Mathew Roy R, Feng X, Wenzel M, Hasse V, Shekhar C, Vergniory M G, Felser C, Pronin A V and Dressel M 2025 *Phys. Rev. Lett.* **135** 116503.

[19] Sun X, Wei Z, Shan M, Peng S, Luo Y, Shen J, Huai L, Miao Y, Ou Z, Onbasli M, Wang Z, Wu T, He J and Chen X H 2025 arXiv:2508.18099 [cond-mat.supr-con].

[20] Almoalem A, Gofman R, Nitzav Y, Mangel I, Feldman I, Koo J, Mazzola F, Fujii J, Vobornik I, Sánchez-Barriga J, Clark O J, Plumb N C, Shi M, Yan B and Kanigel A 2024 *npj Quantum Mater.* **9** 36.

[21] Yang F Z, Zhang T T, Meng F Y, Lei H C, Nelson C, Cai Y Q, Vescovo E, Said A H, Lozano P M, Fabbris G and Miao H 2025 *Phys. Rev. B* **111** L041101.

[22] Ribak A, Skiff R M, Mograbi M, Rout P K, Fischer M H, Ruhman J, Chashka K, Dagan Y and Kanigel A 2020 *Sci. Adv.* **6** eaax9480.

[23] Silber I, Mathimalar S, Mangel I, Nayak A K, Green O, Avraham N, Beidenkopf H, Feldman I, Kanigel A, Klein A, Goldstein M, Banerjee A, Sela E and Dagan Y 2024 *Nat. Commun.* **15** 824.

[24] Nayak A K, Steinbok A, Roet Y, Koo J, Margalit G, Feldman I, Almoalem A, Kanigel A, Fiete G A, Yan B, Oreg Y, Avraham N and Beidenkopf H 2021 *Nat. Phys.* **17** 1413.

[25] Kumar Nayak A, Steinbok A, Roet Y, Koo J, Feldman I, Almoalem A, Kanigel A, Yan B,

Rosch A, Avraham N and Beidenkopf H 2023 *Proc. Natl. Acad. Sci. U.S.A*. **120** e2304274120.
[26] Persky E, Bjørlig A V, Feldman I, Almoalem A, Altman E, Berg E, Kimchi I, Ruhman J, Kanigel A and Kalisky B 2022 *Nature* **607** 692.
[27] Almoalem A, Feldman I, Mangel I, Shlafman M, Yaish Y E, Fischer M H, Moshe M, Ruhman J and Kanigel A 2024 *Nat. Commun.* **15** 4623.
[28] Date M, Bae H, Louat A, Domaine G, Schröter N B M, Da Como E, Yan B and Watson M D 2026 *Commun. Phys*. **9** 60.
[29] Liu B, Li H K, Wu Z M, Han W B, Gao M Y, Wang Y N, Qiu T, Wang J J and Shi Z Z 2025 *J. Alloys Compd.* **1041** 183768.
[30] Hovden R, Tsen A W, Liu P, Savitzky B H, El Baggari I, Liu Y, Lu W J, Sun Y P, Kim P, Pasupathy A N and Kourkoutis L F 2016 *Proc. Natl. Acad. Sci. U.S.A*. **113** 11420.
[31] Lee S H, Goh J S and Cho D 2019 *Phys. Rev. Lett.* **122** 106404.
[32] Cheng L, Nie L P, Long X Y, Liang L, Zhao D, Li J, Liu Z, Wu T, Chen X H, Duan W H and Zou X L 2023 *Phys. Rev. Mater*. **7** L091001.
[33] Xu S X, Deng J Z, Gao J J, Meng F Y, Shi L F, Yang P T, Wang N N, Liu Z Y, Sun J P, Uwatoko Y, Lei H C, Luo X, Sun Y P, Wang N L, Wang Z J, Wang B S and Cheng J G 2024 *Phys. Rev. B* **109** 144522.
[34] Gao J J, Si J G, Luo X, Yan J, Jiang Z Z, Wang W, Han Y Y, Tong P, Song W H, Zhu X B, Li Q J, Lu W J and Sun Y P 2020 *Phys. Rev. B* **102** 075138.
[35] Xu J, Wang Y, Pate S E, Zhu Y L, Mao Z Q, Zhang X F, Zhou X Q, Welp U, Kwok W K, Chung D Y, Kanatzidis M G and Xiao Z L 2023 *Phys. Rev. B* **107** 035104.
[36] Smink A E, De Boer J C, Stehno M P, Brinkman A, Van Der Wiel W G and Hilgenkamp H 2017 *Phys. Rev. Lett.* **118** 106401.
[37] Geng Y Y, Guo J F, Meng F Y, Wang M Y, Mi S, Huang L, Xu R, Pang F, Liu K, Wang S C, Gao H J, Zhou W C, Ji W, Lei H C and Cheng Z H 2024 *Phys. Rev. B* **110** 115107.
[38] Wu P, Wang Z Y, Zhang Y M, Chen Z Y, Yu S K, Ma W R, Shan M, Liang Z Y, Wei X Y, Wang J Z, Cheng W L, Liang Z W, Zhang X C, Wu T, Okada Y, Jiang K, Wang Z Y and Chen X H 2025 arXiv:2508.17861 [cond-mat.supr-con].
[39] Yeh P C, Jin W, Zaki N, Kunstmann J, Chenet D, Arefe G, Sadowski J T, Dadap J I, Sutter P, Hone J and Osgood R M Jr 2016 *Nano Lett*. **16** 953.
[40] Pei D, Zhou Z, He Z, An L, Gao H, Xiao H, Chen C, He S, Barinov A, Liu J, Weng H, Wang N, Liu Z and Chen Y 2023 *Nano Lett*. **23** 7008.
[41] Zhang C, Chuu C P, Ren X, Li M Y, Li L J, Jin C, Chou M Y and Shih C K 2017 *Sci. Adv.* **3** e1601459.
[42] Tran K, Moody G, Wu F, Lu X, Choi J, Kim K, Rai A, Sanchez D A, Quan J, Singh A, Embley J, Zepeda A, Campbell M, Autry T, Taniguchi T, Watanabe K, Lu N, Banerjee S K, Silverman K L, Kim S, Tutuc E, Yang L, MacDonald A H and Li X 2019 *Nature* **567** 71.
[43] Shen S, Qin T, Gao J J, Wen C H, Wang J H, Wang W, Li J, Luo X, Lu W J, Sun Y P and Yan S C **2022** *Chin. Phys. Lett.* **39** 077401.